Chapter 5

Potassium doped LaCoO$_3$ Perovskite; La$_{1-x}$K$_x$CoO$_{3-\delta}$ (0≤x≤0.5): A Novel Bifunctional OER catalyst and supercapacitive energy storage material

5.1 Introduction

Due to increasing environmental pollution issues and the emergence of an electrified society, the demand for energy storage and delivery technologies through ever-fluctuating renewable energy resources is increasing.[1] Redox chemistry provides the fundamental basis for numerous energy-related electrochemical devices.[2] A crucial part is the discovery of efficient and cost-effective catalytic elements for usage in electrochemical energy conversion processes [3] and storage devices[4]. Hydrogen fuel and oxygen are produced from the electrolysis of water in the presence of an electrocatalyst. On the other hand, supercapacitors can fill up the fast rechargeability energy storage problem with a long cycling life achieving a high power density, and also solve the lower risk of fire or explosion in comparison to widely used batteries.[6] It will be highly interesting if a low-cost single material can be developed, which has both properties (energy conversion and storage). Some specific transition-metal oxides (TMOs) could be highly successful because of their intrinsic properties such as amalgamation of charge storage behaviour, oxygen evolution ability from water, and their multifold advantages including excellent high metal ion reactivity, electrochemical stability, and low cost.[1,2,6,7] The transition metal (Fe, Co, Ni, and Mn) oxides have superior reversible surface redox (faradaic) behaviour and have a promising catalytic property, for this reason, they are most suitable for electrode materials for energy storage (supercapacitors, batteries) [8] as well as efficient co-catalysts for production devices (water electrolysis, fuel cells)[9] The state-of-the-art (structure and high electrical conductivity) electrocatalysts RuO$_2$ and IrO$_2$ have excellent OER activities in both alkaline and acidic media. [10-11]Multi-function transition metal-based materials show excellent energy conversion and energy storage

properties including oxides (2D δ-MnO_2 [12], NiO[13-14] $ZnCo_2O_4$ [15], $NiCo_2O_4$ [16] β-$NiMoO_4$[17]) hydroxides (FeNi LDH/GO hybrid [18] NiFe-LDH [19], CoNiFe layered double hydroxides [20]), sulfides (FeS[21] and MoS_2,[22] CoS[22] and CuS[22]) and so forth. Perovskites type (ABO_3) structural of metal oxide materials have excellent posterities because they exhibit greater cation ordering and order channels of oxygen vacancies resulting in the fast mobility of oxygen ions (O^{2-}) that improve both energy conversion (OER(oxygen Evolution Reaction) and ORR(oxygen Reduction Reaction)). [23-26] The e_g electron points directly towards the surface O atom and plays an important role during O_2^{2-}/OH^- exchange. The e_g orbital filling was established as an OER/ORR activity determining parameter with optimal e_g orbital occupancy close to 1 and the $Ba_{0.5}Sr_{0.5}Co_{0.8}Fe_{0.2}O_{3-\delta}$ with nearly e_g^1 configuration was shown as a superior OER catalyst and also applicable for best ORR catalyst, $LaMnO_{3+\delta}$ where e_g is also close to 1. Sabatier's principle explains that superior catalytic activity can be achieved when adsorbed species lightly bind to the surface neither so strongly nor too weakly. But the binding strength of oxygen molecules and reaction intermediates is hard to obtain experimentally[23-26]. Structure e_g electron plays a crucial role in energy storage like pseudocapacitors application in the perovskite-type structure. John-teller distortion is found in octahedral symmetry when e_g electron close to 1 and enhances pseudocapacitors performance. Perovskite materials have also superior electrical and electronic properties that can be tuned systematically by cation substitutions on both the A and B sites with different valance states and ionic sizes. [27-41]

In this chapter, I present the synthesis, and characterization of $La_{1-x}K_xCoO_{3-\delta}$ (0≤x≤0.5) Perovskite and its electrochemical performances in the term of supercapacitive charge storage in neutral 0.5M $NaSO_4$ electrolyte and an efficient OER/ORR electrocatalyst in 1M KOH electrolyte. The study also determines the role or tuning of oxygen vacancies with doping K ion in $LaCoO_3$ resulting in novel electrocatalytic and energy conversion and storage properties.

5.2 Materials Synthesis and characterizations:

The sol-gel auto combustion synthesis route was utilized to synthesize crystalline A series of perovskite oxides, K doped $La_{1-x}K_xCoO_{3-\delta}$ (x = 0, 0.1, 0.2, 0.3, 0.4, 0.5).

Ethylene glycol was used as fuel, Lanthanum (III) nitrate hexahydrate (La(NO$_3$)$_3$.6H$_2$O) (99.8), KNO$_3$ (99.9%), Cobalt (II) nitrate hexahydrate (Co(NO$_3$)$_2$.6H$_2$O) (99.9%) were used as the precursors and were dissolved in deionized water. The mixture was magnetically stirred at 120^{0}C for 5 hours to form a wet gel, The obtained xerogel was calcined at 400 ^{0}C for 3 h to remove organic impurities, then calcinations at 1050 °C for 12 h to form the final single-phase perovskite of La$_{1-x}$K$_x$CoO$_{3-\delta}$ (x = 0.1, 0.2, 0.3, 0.4, 0.5) material.

The phase purity was examined through Rigaku Miniflex desktop X-ray Diffractometer (XRD) with Cu-Kα radiation (λ = 1.54 Å) in the range 2θ ∼ 20 - 90° with a step size of 0.02°. The structures were refined by the Rietveld method using FULLPROF suite software. Pore size distribution and specific surface area of the materials were measured by BET MicrotracBEL under an N$_2$ atmosphere. The microstructures of the sintered materials were examined by using a scanning electron microscope (SEM) (Model: EVO - Scanning Electron Microscope MA15/18). The average grain size was calculated from the SEM images using the linear intercept method. The compositions of the materials were examined by the energy-dispersive X-ray (EDX) method with a probe attached to the SEM instrument. X-ray Photo-electron Spectroscopy (XPS) studies were carried out to examine the electronic states of the materials. XPS of the samples were collected using Thermo Scientific Multilab 2000 instrument by employing Al (Kα) radiation source operated at 150 kW. Binding energies were corrected and reported here concerning C (1s) at 284.5 eV and they are accurate within ±0.1 eV.

5.2.1 Electrode fabrication

The electrochemical measurements were carried out using nova 2.0 auto lab. The catalyst ink was prepared by homogenizing 35 mg of catalyst, 10 mg of acetylene black, and 5 mg PVDF binder in 1 mL of NMP solvent under an ultra-sonication bath for 40 min. To investigate the activity of the OER/ORR and electrochemical charge storage, an aliquot of 20 μL of homogenized ink was deposited by a micropipette onto the surface of a carbon paper (Torrey carbon paper, Alfa Aesar) (1x1 cm^2 area) and dried under an IR lamp. The electrode loading was calculated by taking the weight of the electrode through electronic balance (error limit: 0.01mg). For that, the first weight of Torrey paper was taken then the weight of coated electrode (after drying the

coated ink on Torrey carbon paper on a 1x1 cm^2 area was taken for the study. Then from the difference in the weight, the exact loading of electrode material was calculated. The total material load was typically 1mg (0.7mg active material: carbon: PVDF binder). Both electrocatalytic (OER and ORR) performances and supercapacitive charge storage measurements were carried out by depositing the perovskite materials on the same carbon paper (Torrey carbon paper, Alfa Aesar) for electrode preparation.

5.2.2 Electrochemical Studies:

All electrochemical measurements were carried out by employing Metrohm Autolab (PGSTAT204) instrument an equipped with FRA32M module. Electrochemical data were analyzed using NOVA 2.0 software

5.2.2.1 Electrocatalysts measurement

Cyclic voltammetry (CV), linear sweep voltammetry (LSV), and electrochemical impedance spectroscopy (EIS) at frequencies of 0.01-100 kHz were carried out in a conventional three-electrode arrangement to examine the electrochemical characteristics of the prepared Pt was used as a counter-electrode and Hg/HgO in 1 M KOH was utilized as a reference electrode. All the potential windows and electrode potentials of the electrocatalyst presented in this chapter are concerning Hg/HgO in the 1M KOH electrode.

Electrode potential conversions/calculations for the overpotential measurements were carried out using the following equations.

$E_{RHE} = E_{Hg/HgO} + E^o_{Hg/HgO} + 0.059pH$ ($E^o_{Hg/HgO}$ =0.098 for 1 M KOH)

$$(5.1)$$

$Overpotential = E_{RHE} - 1.23 - iR$

$$(5.2)$$

Resistance (R) is calculated using EIS measurements. Oxygen-saturated 1 KOH solution was used as the electrolyte in the study. In this work, all electrochemical experiments were carried out with IR compensation. The electrolyte solutions were

freshly prepared before each set of investigations using analytical grade KOH (Lachner, Czech Republic) and triply distilled deionized water.[42]

5.2.2.2 Supercapacitors measurement

Pt was used as a counter-electrode and Hg/HgO (1M KOH) was utilized as a reference electrode. All electrodes were measured in 0.5M Na_2SO_4 electrolytes. Cyclic voltammetry (CV) was used to show redox behaviour, Chronopotentiometry was used for charge-discharge capacity measurements and EIS at frequencies of 0.01-100 kHz was used for overall internal resistance measurements.

5.3 Results and discussions:

5.3.1 Crystallographic characterization

Powder XRD patterns of sol-gel auto-combustion synthesized $La_{1-x}K_xCoO_{3-\delta}$ ($0 \leq x \leq 0.5$) perovskite cobaltates are shown in **Figure 1. (a)**. All the synthesized materials show a single-phase formation. The prominent single-phase diffraction peak matches well with the JCPDS file: (JCPDS 1048-0123). Powder XRD patterns of sol-gel auto-combustion synthesized $La_{1-x}K_xCoO_{3-\delta}$ ($0 \leq x \leq 0.5$) perovskite cobaltates are shown in **Figure 5.1. (a)**. All the synthesized materials show a single-phase formation. The prominent single-phase diffraction peak matches well with the JCPDS file: (JCPDS 1048-0123) and shows peaks shift with doping K+ ion in $LaCoO_3$ perovskite lattice . Rietveld refined XRD profile of
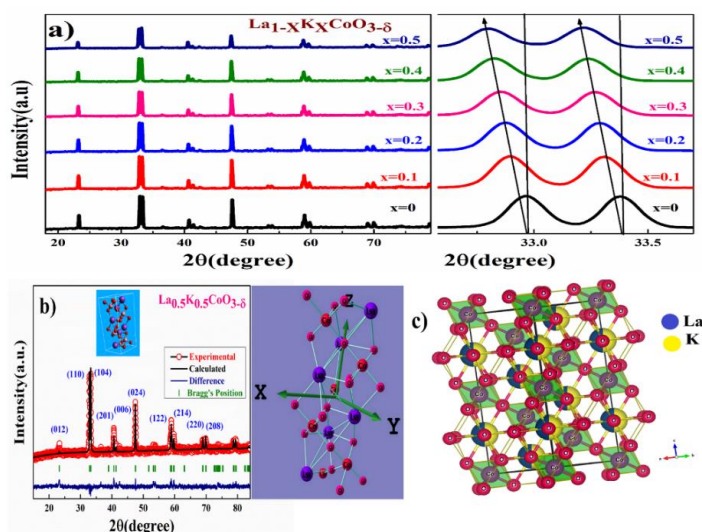
Figure 5. 1 (a) XRD pattern of $La_{1-x}K_xCoO_{3-\delta}$ ($0 \leq x \leq 0.5$), (b) Rietveld refinement of $La_{.5}K_{.5}CoO_{3-\delta}$, (c) vesta image of $La_{.5}K_{.5}CoO_{3-\delta}$

$La_{0.5}K_{0.5}CoO_{3-\delta}$ is provided in **Figure 5.1 (b)**. Rietveld refinement studies of $La_{1-x}K_xCoO_{3-\delta}$ ($0 \leq x \leq 0.5$) XRD pattern in the product oxide could be indexed in rhombohedral (hexagonal setting) in the R-3c space group (No. 167). Structural parameters derived from Rietveld refinement are presented in **Table 5.1.** The (110)/ (104) peak (highest intensity peak) shifted linearly to a higher 2θ value with increasing dopant (K^+ ion) concentration on the La site. As ionic radii of K^+ (1.64 Å, 12 coordination) is greater than La^{3+} (1.36 Å, 12 coordination), [43] doping of K on the La site will result in peak shifting to a lower 2θ value. **Figure 5.1 (c) vesta image of** $La_{0.5}K_{0.5}CoO_{3-\delta}$ **sample**

Table 5.1 lattice parameter of $La_{1-x}K_xCoO_{3-\delta}$ ($0 \leq x \leq 0.5$)

| Sample	a=b (A^0)	c(A^0)	$\alpha=\beta=$ (^{0})	γ (^{0})	Chi^2	R_{bragg}	R_f	R_{wp}
$LaCoO_3$	5.4485(8)	13.1042(4)	90	120	2.4	1.18	2.64	5.36
$La_{0.9}K_{0.1}CoO_{3-\delta}$	5.4484(4)	13.1040(2)	90	120	3.34	2.94	4.63	5.8
$La_{0.8}K_{0.2}CoO_{3-\delta}$	5.4483(5)	13.1039(3)	90	120	3.62	3.63	5.68	6.4
$La_{0.7}K_{0.3}CoO_{3-\delta}$	5.4483(4)	13.1038(5)	90	120	3.87	4.46	6.33	6.9
$La_{0.6}K_{0.4}CoO_{3-\delta}$	5.4482(3)	13.1038(3)	90	120	4.45	5.42	6.76	6.97
$La_{0.5}K_{0.5}CoO_{3-\delta}$	5.4481(2)	13.1037(4)	90	120	4.83	5.87	7.44	7.11

5.3.2 FTIR spectra analysis

Figure 5.2 shows the FTIR spectra of $La_{1-x}K_xCoO_{3-\delta}$ (x = 0, 0.3 and 0.5) perovskite-type oxides. Two types of vibration bands appeared in the IR spectra of all $La_{1-x}K_xCoO_{3-\delta}$ (x = 0, 0.3, and 0.5) samples. The vibration band at 456.30 cm^{-1} belongs to the bending vibration of O-Co-O bonding in the BO_6 octahedron in $LaCoO_3$ and whereas in $La_{0.7}K_{0.3}CoO_{3-\delta,}$ the bands are shifted to a comparatively lower value at 442.44 cm^{-1}. The O-Co-O band bending is invisible, maybe the sign of distortion of BO_6 octahedra due to incorporation in K ion in the lattice and formation of BO_5 octahedron. [44] It is observed from FTIR spectra of the doped sample, that the infrared

absorption bands at a higher frequency are progressively shifted from 456 cm^{-1} for LaCoO$_3$ to the lower frequency (442.44 cm^{-1}) for La$_{0.7}$K$_{0.3}$CoO$_{3-\delta}$. Based on the force constant phenomenon, the La^{3+} ion (1.10) is more electronegative than the K$^+$ ion (0.8). When increasing the K ions doping more than 30% band bending become invisible compared to the unsubstituted LaCoO$_3$ sample, the band at 712.47 cm^{-1} become broad and upshifting suggesting that some amounts of Co^{3+} changed into Co^{4+} when some La^{3+} was replaced by K$^+$. The interaction between Co^{4+} and O is stronger than that of Co^{3+} and O, and thus the wave number of the stretching vibration of Co^{4+}-O is greater than that of Co^{3+}–O. Therefore, the upshifting of the wave number of stretching vibration of the Co–O bond in the BO$_6$ octahedron may suggest the formation of some Co^{4+} in the La$_{1-x}$K$_x$CoO$_{3-\delta}$ lattice. [45-46]
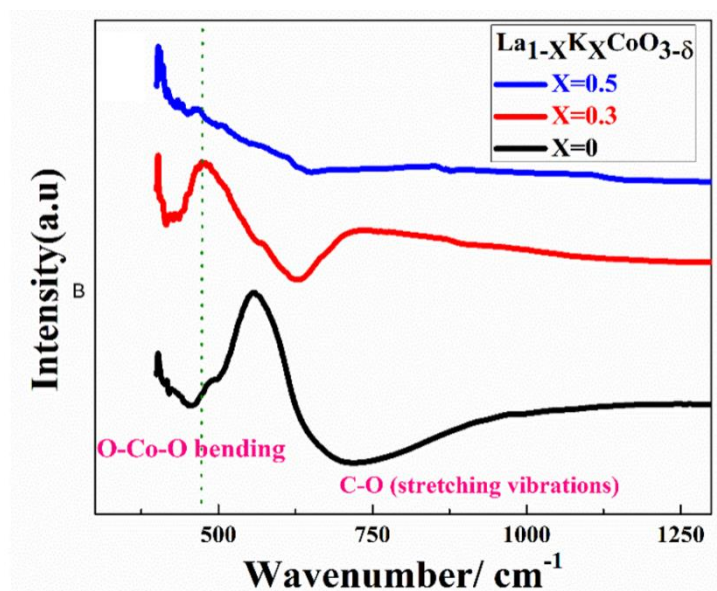
Figure 5.2 FTIR spectra of La$_{1-x}$K$_x$CoO$_{3-\delta}$ (x=0, 0.3, 0.5)

5.3.3 UV-vis absorption spectrum and bandgap analysis
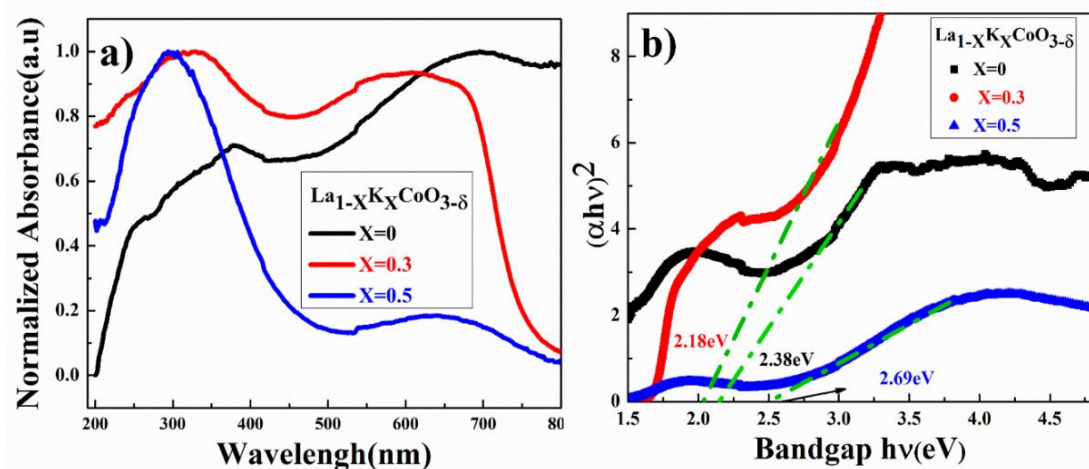
Figure 5.3 (a) UV-vis absorption spectrum of $La_{1-x}K_xCoO_{3-\delta}$ (x=0, 0.3, 0.5) (b)) Optical bandgap of $La_{1-x}K_xCoO_{3-\delta}$ (x=0, 0.3, 0.5).

Figure 5.3 (a) shows UV-vis absorption spectrum of $La_{1-x}K_xCoO_{3-\delta}$ (x = 0, 0.3 and 0.5) powder sample. **Figure 5.3 (b)** shows bandgap decreases with an increase of K concentration up to 30%, from 2.68 eV to 2.18 eV. Further with increasing K concentration and bandgap decrease only to 2.38 eV for the $La_{0.5}K_{0.5}CoO_{3-\delta}$ sample

5.3.4 BET surface area and pore size analysis

. N_2 adsorption-desorption isotherms with pore size distribution are shown for $LaCoO_3$, $La_{0.7}K_{0.3}CoO_{3-\delta}$, and $La_{0.5}K_{0.5}CoO_{3-\delta}$ as shown in **Figure 5.4** The surface area was found to be 19m^2/g, 24m^2/g, and 29m^2/g for $LaCoO_3$, $La_{0.7}K_{0.3}CoO_{3-\delta}$, and $La_{0.5}K_{0.5}CoO_{3-\delta}$ samples respectively, The pore size distribution curve presented in the insert of those samples, and the pore diameter was found to be 21nm, 23nm 27nm respectively for $LaCoO_3$, $La_{0.7}K_{0.3}CoO_{3-\delta}$, and $La_{0.5}K_{0.5}CoO_{3-\delta}$ samples. This indicates that with increasing K concentration, surface area and pore diameters are increasing. Due to large difference in ionic radii of La^{3+} and K^+ ion, high residual stress (peak broadening) can be generated with doping of higher concentration of K^+ ion at La^{3+} site, resulting smaller crystallites. Smaller the crystallite size, higher the surface area of the material
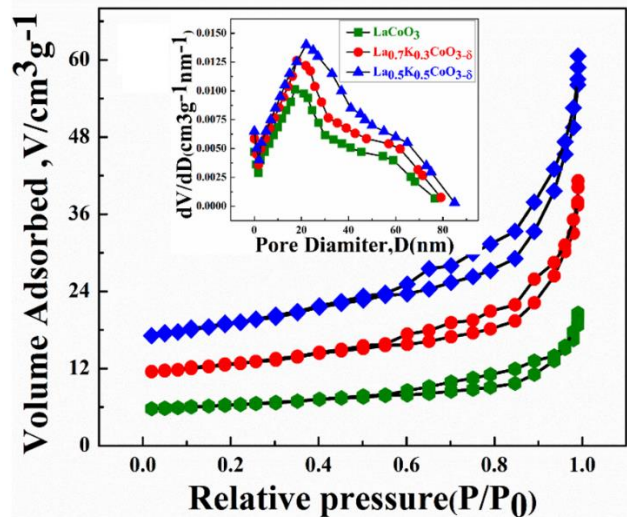
**Figure 5.4** N_2 adsorption/desorption isotherms of $La_{1-x}K_xCoO_{3-\delta}$ (x=0, 0.3, 0.5)

5.3.5 XPS analysis

Survey spectra of $La_{0.5}K_{0.5}CoO_{3-\delta}$ sample containing (C1s), O(1s), Co(2p), La(3d), K(2s) (377.32eV) ,and K(2p) (293.3eV)[27,47] is shown in **Figure 5.5.(a)**. To investigate the Co oxidation state, XPS of core level Co(2p) spectra of $La_{0.5}K_{0.5}CoO_{3-\delta}$ sample are deconvoluted and shown in **Figure 5.5. (b).** XPS curve is fitted or deconvoluted with the help of XPSPEAK41 software. The peak position indicates that only the Co^{3+} (t_2g^5 eg^1) state is present in $LaCoO_3$ and both Co^{3+}((t_2g^5 eg^1))and Co^{4+}(t_2g^4 eg^1) states are presented in $La_{0.5}K_{0.5}CoO_{3-\delta}$. For Co^{3+} oxidation state, binding energies were obtained at 779.38eV (2p3/2) and 794.95 eV (2p1/2) and for Co^{4+} oxidation state, binding energies were obtained at 780.83 eV (2p3/2) and 796.57eV (2p1/2) with the presence of a weak satellite peak at 784.34 eV corresponding to Co^{4+} , 790.32 eV corresponding to Co^{3+} and 803.15eV corresponding to Co^{4+}/Co^{3+}. Co ($2p_{3/2, 1/2}$) spectrum depicts the presence of Co^{4+} ion as the majority phase in $La_{0.5}K_{0.5}CoO_{3-\delta}$. Co^{4+} and Co^{3+} ions ratio were calculated from their peak strength and Co^{4+} and Co^{3+} ions were found in the ratio of 63:37 in the materials. **Figure 5.5. (c)** shows a comparative the O(1s) spectrum of $LaCoO_3$, $La_{0.7}K_{0.3}CoO_{3-\delta}$, and $La_{0.5}K_{0.5}CoO_{3-\delta}$ samples containing two types of binding energies respectively at O1s (lattice Oxygen) and O1s (adsorbed Oxygen) due to difference in the bonding strength as two distinctive Co^{4+} (t_2g^4 eg^1) and Co^{3+} (t_2g^4 eg^1) ions present in the same materials.
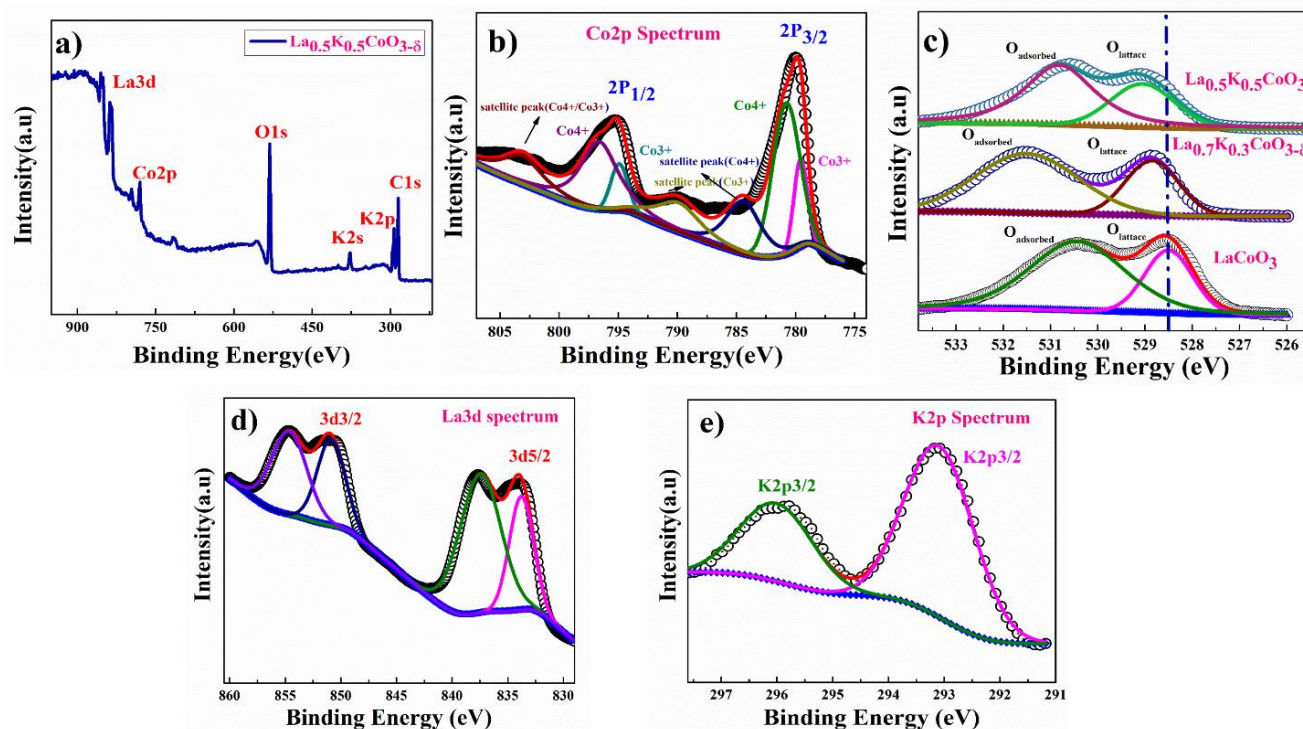
Figure 5. 5 XPS of La$_{0.5}$K$_{0.5}$CoO$_{3-\delta}$ of powder sample (a) full survey, (b) Fe(2p) core level, (c) O(1s), (d) La (3d) and (e) K(2p)

An increase in the intensities of O1s (adsorbed Oxygen) indicates the formation of more Oxygen vacancies with increasing the concentration of K ion in the LaCoO$_3$ lattice.[48] **Figure 5.5. (d)** Shows La (3d) spectrum presenting two sets of La(3d)5/2 and La(3d)1/2 peaks at (833.91eV and 851.02eV) and (837.27 eV and 854.59eV) respectively due to its bonding with two different type of Co-O octahedral. **Figure 5.5. (e)** shows K (2p) $_{3/2, \; 1/2}$ spectra, at 293.14eV and 296.03 eV respectively.

5.3.6 SEM analysis

The **SEM** image is shown in **figure 5.6. (a)** presents the slightly rectangular porous type particle morphology of the La$_{0.5}$K$_{0.5}$CoO$_{3-\delta}$ sample. Particle size distribution was calculated by **ImageJ** software. Particle size distribution was fitted with Gaussian distribution, and particle diameter was found in the range of 2μm to 4.5 μm with an average particle diameter of about 2.9 μm. **Figure 5.6. (b)** represent EDX of La$_{0.5}$K$_{0.5}$CoO$_{3-\delta}$ powder, where K, La, Co, and O are present in the required ratio.
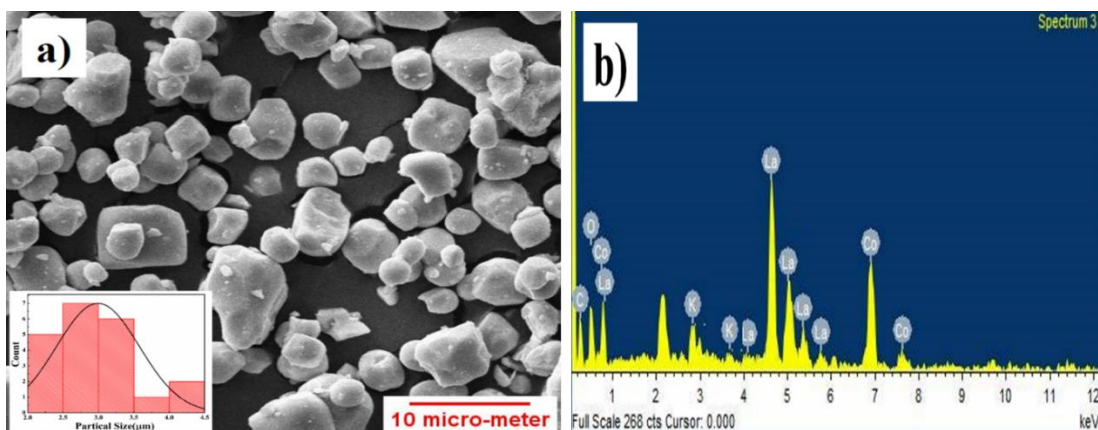
Figure 5.6 (a) SEM image showing particle distribution of $La_{0.5}K_{0.5}CoO_{3-\delta}$ (c) EDX elemental analysis of $La_{0.5}K_{0.5}CoO_{3-\delta}$

5.3.7 TEM analysis

Figure 5.7. (a-b) shows HRTEM images of $LaCoO_3$ and $La_{0.5}K_{0.5}CoO_{3-\delta}$ samples. Lattice fringes are visible in the inverse Fast Fourier transform (FFT) (mapping with Gatan Digital micrograph software) of this region, confirming the crystalline nature of $LaCoO_3$ and $La_{0.5}K_{0.5}CoO_{3-\delta}$. Lattice fringe spacing is in agreement with interplanar spacing obtained from XRD results. HRTEM images exhibited lattice fringe spacing of d = 0.377 nm and 0.385 nm for pure $LaCoO_3$ and $La_{0.5}K_{0.5}CoO_{3-\delta}$ respectively, corresponding to the (012) crystal plane of the perovskite structure (JCPDS card No. 86-1663). The d spacing is increased with an increase in the K^+ ion concentration in the $LaCoO_3$ lattice
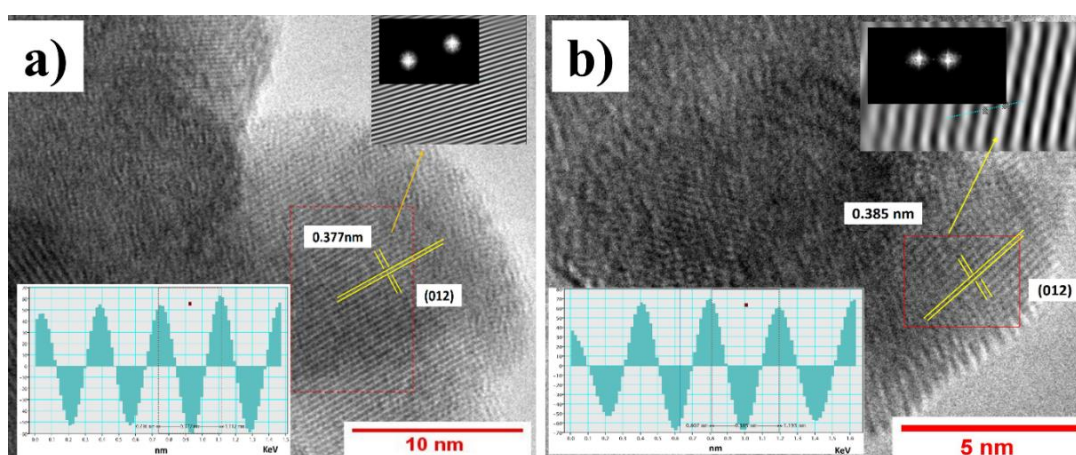
Figure 5.7 (a) TEM image along with HRTEM showing lattice fringes and high-resolution FFT, inverse FFT with d spacing (012 planes) of $LaCoO_3$. (b) TEM image along with HRTEM showing lattice fringes and high-resolution FFT, inverse FFT with d spacing (012 planes) of $La_{0.5}K_{0.5}CoO_{3-\delta}$

133

5.3.8 Strain-induced distortion of CoO₅ octahedra

Figure 5.8 shows the strain-induced distortion of CoO₅ octahedra due to the incorporation of monovalent K^+ ion in the $LaCoO_3$ lattice that introduces oxygen vacancy in the lattice. This distortion favours the in-situ formation of intermediate spin (IS) Co^{4+} (electronic configuration: $t_{2g}^4 e_g^1$) ions to support the Jahn-Teller distortion. Similarly, the existence of intermediate spin Co^{3+} ($t_2g^5 eg^1$) and/or Co^{4+}($t_2g^4 eg^1$) in the perovskite lattice is known to enhance the electrocatalytic activity and electronic structure and crystal structure of perovskite oxides, thereby making themselves suitable for the superior electrocatalytic activity toward OER and ORR. [39, 40, 49-51]
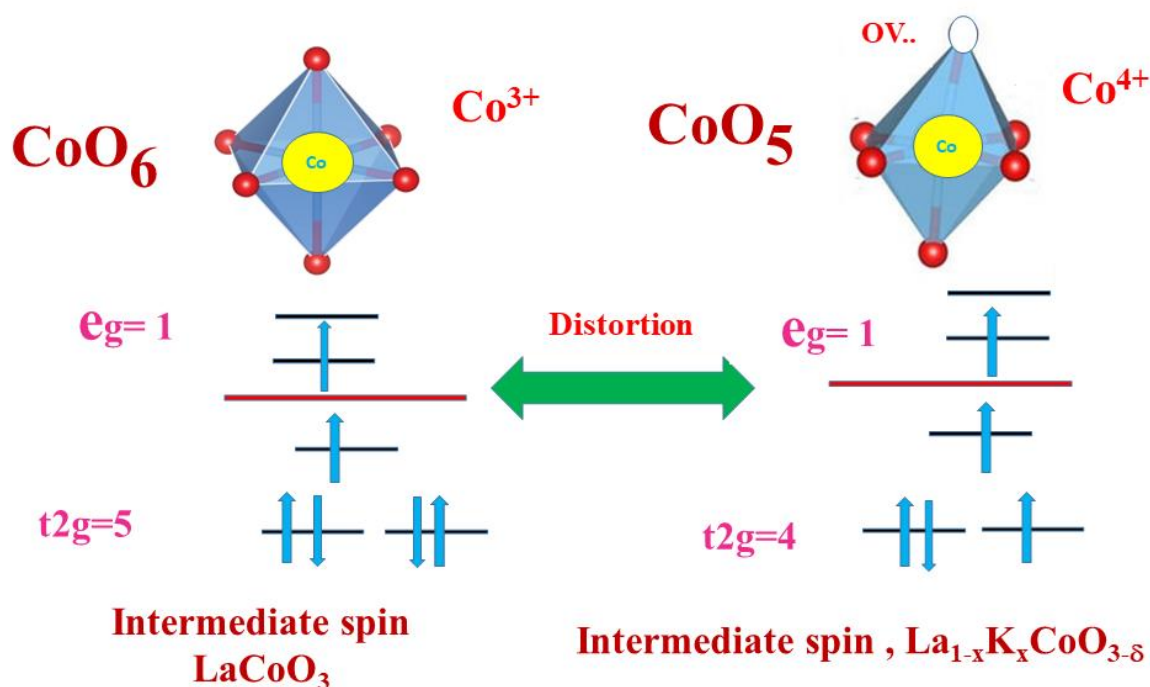

Figure 5.8 Scheme showing the presence of oxygen vacancies BO₅ octahedral

5.3.9 Double-exchange of Co³⁺-O²⁻ -Co⁴⁺

Figure 5. 9 shows a double-exchange of $Co3^+$-O^{2-} -Co^{4+} interaction in the $La_{1-x}K_xCoO_{3-\delta}$ ($0 \leq x \leq 0.5$) samples**.** The amount of K^+ ions increased and that of La^{3+} ions decreased at the A-sites, which introduces strain in the $La_{1-x}K_xCoO_{3-\delta}$ ($0 \leq x \leq 0.5$). The difference between the average ionic radii of the ions present at the A-site ions increases with an increase in K^+ ion doping which introduces tensile stress

variations, that make CoO_6 octahedra distorted and rotated, by the migration of itinerant electrons between Co^{3+} and Co^{4+} ions using O^{2-} ions as a bridge, and increases the hopping conductivity. But above 30% of K of doping, the double exchange in the $Co3^+$-O^{2-}-Co^{4+} pair is decreased due to an increase in oxygen vacancies in the lattice that resulted in again increase in the resistivity of $La_{0.5}K_{0.5}CoO_{3-\delta}$ as confirmed by the XPS, IR and UV-visible spectroscopy studies.[52]
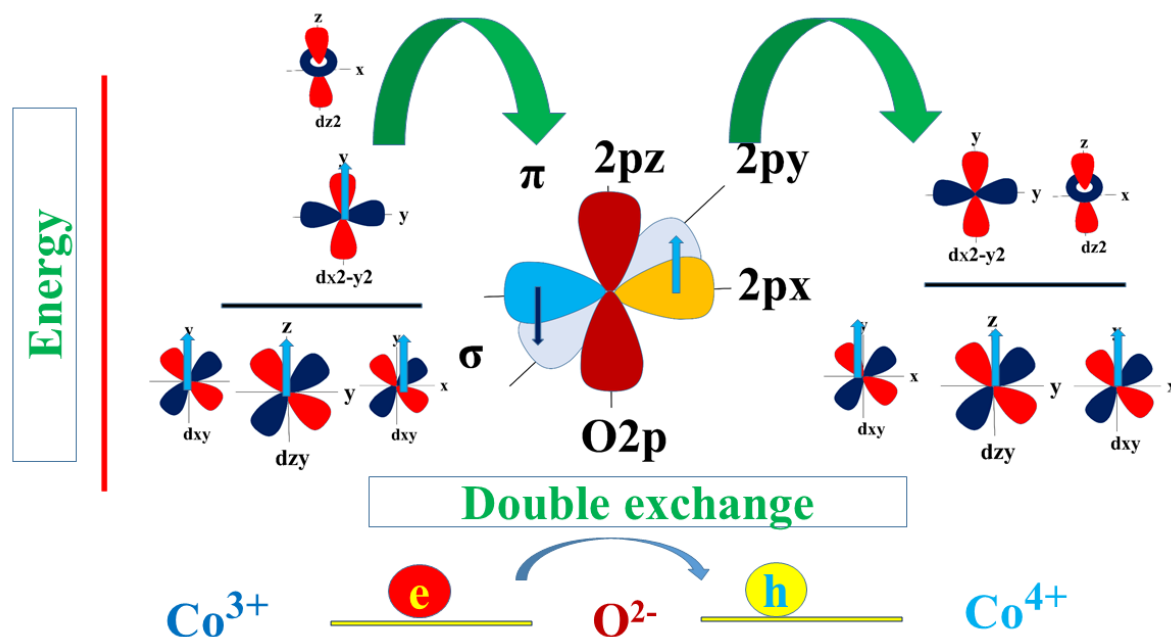

Figure 5.9 Atomic orbital diagram of double-exchange Co^{3+} –O^{2-} -Co^{4+} interaction

5.3.10 Co(3d)/O(2p) orbital overlap

Figure.5.10 shows the increase in Co(3d)/O(2p) orbital overlap (covalency increases) that results in higher covalency in Co-O bond resulting in the formation of ligand hole due to a decrease in Fermi level position coupled with Co(3d)/O(2p) π^* band formation. Thus pinning of Fermi level due to oxygen vacancies at the top of the Co(3d)/O(2p) π^* band results in higher ligand hole concentration required for superior OER activity.[39,53] Overlap is increased up to 30% K doped in $LaCoO_3$ lattice, as supported by FT-IR and UV-visible spectroscopy as the lowest bandgap (2.18eV) in the $La_{1-x}K_xCoO_{3-\delta}$ series was is was found for 30% K doped $LaCoO_3$ sample as shown in **Figure 5.3**

As shown by XPS studies earlier, due to the presence of Co^{3+} and Co^{4+} in the $La_{1-x}K_xCoO_{3-\delta}$ sample, the catalytic activity due to the participation of active metal redox ($Co^{3+/4+}$), as well as electronic and ionic properties of the material, are feasibly enhanced. Similarly, the existence of intermediate spin Co^{3+} (t_2g^5 eg^1) and/or Co^{4+}(t_2g^4 eg^1) in the perovskite lattice is known to enhance the electrocatalytic activity for both ORR and OER.[39,51] A model of such an active electrocatalyst oxide surface is established; in the oxygen, vacant BO_5 octahedra containing surface oxygen vacancy, the 3d orbital (e_g and t_{2g}) energy split further due to lower symmetry near the surface resulting in more active sites for the reaction of $La_{1-x}K_xCoO_{3-\delta}$ type oxygen vacant perovskite.
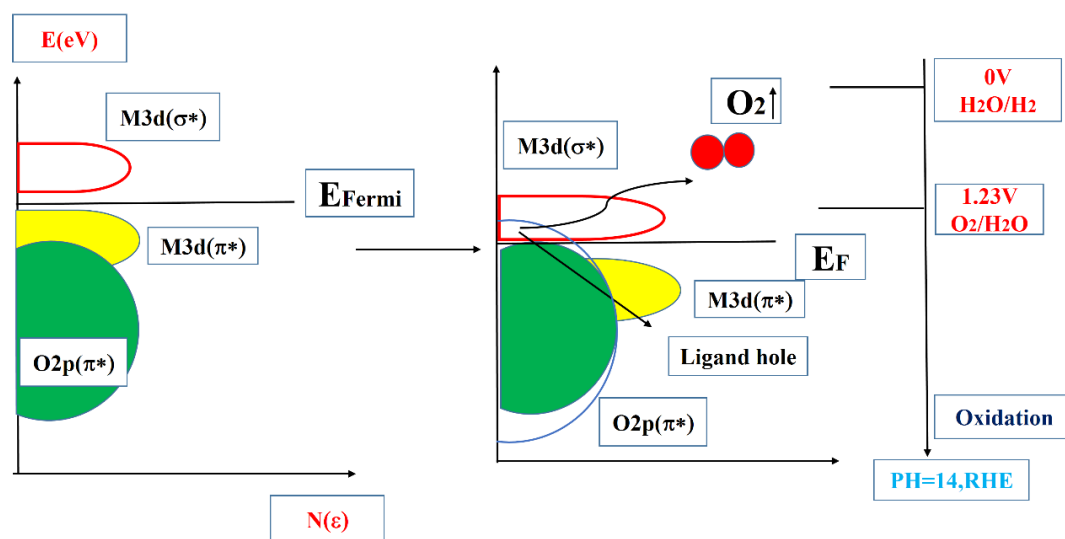
Figure. 5.10 Oxygen Vacancies pinning Fermi level at the top of the Co(3d)/O(2p) π* band

5.3.11 Mott–Schottky plot

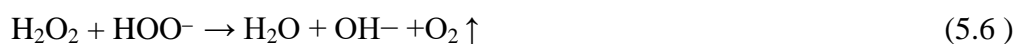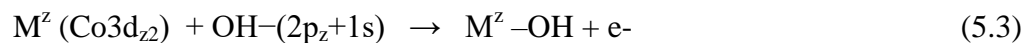**Figure 5.11** shows Mott–Schottky plot at 1KHz in between 0 to -1V, the negative slope of the Mott–Schottky plot denotes that $La_{1-x}K_xCoO_{3-\delta}$ ($0 \leq x \leq 0.5$) materials are p-type (hole) semiconductors. Flat band (E_{fb}) potential is an applied potential at which the Fermi level is pinned at the same energy near the electrolyte redox potential. E_{fb} is an important parameter that provides basic information about the electrochemical interface potential between the electrode and the electrolyte.[43, 45] As shown in **Figure. 5.10**, the flat band (E_{fb}) potential calculated for $La_{0.7}K_{0.3}CoO_{3-\delta}$ are found to be 1.534V verse RHE in 1M KOH electrolyte
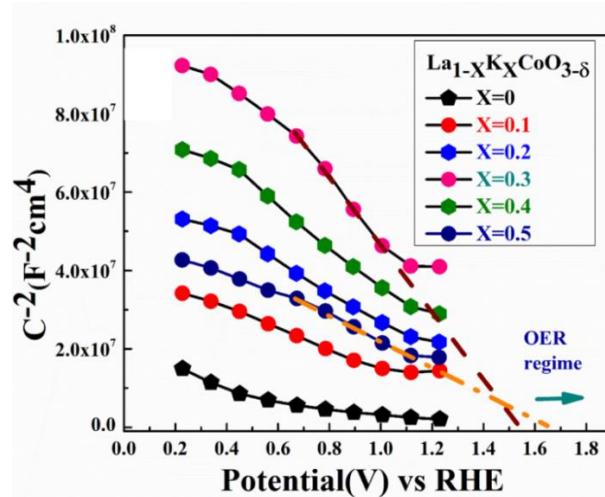
Figure. 5.11 Mott–Schottky plot of p-type (hole) semiconductor $La_{1-X}K_XCoO_{3-\delta}$ ($0 \leq x \leq 0.5$) and Flat band (E_{fb}) potential.

5.3.12 Linear Sweep Voltammetry (LSV) analysis

. **Figure. 5.12(a)** shows a comparative study of OER performances of $La_{0.7}K_{0.3}CoO_{3-\delta}$, $Ba_{0.5}Sr_{0.5}CoO_{3-\delta}$, and BSCF ($Ba_{0.5}Sr_{0.5}Co_{0.8}Fe_{0.2}O_{3-\delta}$) a well-known model electrocatalyst for OER. All the experiments were carried out in oxygen saturated in 1 M KOH at a 3mV/s scan rate and the overpotential for BSCF, $Ba_{0.5}Sr_{0.5}CoO_{3-\delta}$, and $La_{0.7}K_{0.3}CoO_{3-\delta}$ were found to be 281 mV, 315mV and 335 at 10mA/cm^2 current rate.[40] OER is a charging process, during this process, OH^-/O^{2-} ions are oxidized to O_2 and ORR is discharging process where Oxygen gas is reduced to OH^-/O^{2-} using an electrocatalyst mounted at the cathode material in the metal-air battery.[54] OER Mechnamism proposed by Bockris on transition metal in perovskite is given below.[55]

$$M^z (Co3d_{z2}) + OH-(2p_z+1s) \rightarrow M^z-OH + e- \tag{5.3}$$

$$M^z-OH + OH^- \rightarrow Mz-H_2O_2 + e^- \tag{5.4}$$

$$H_2O_2 + OH^- \rightarrow HOO^- + H_2O \tag{5.5}$$

$$H_2O_2 + HOO- \rightarrow H_2O + OH- + O_2\uparrow \tag{5.6}$$

Figure. 5.12 (b) shows Linear sweep voltammogram cycles of $La_{1-x}K_xCoO_{3-\delta}$ ($0 \leq x \leq 0.5$) in 1M KOH at pH=14 for the OER process. It was observed that incorporation of K ion in $La_{1-x}K_xCoO_{3-\delta}$ ($0 \leq x \leq 0.5$) lattice, up to 30% K doped decreases the onset potential From 1.639V for $LaCoO_3$ to the lowest onset potential of 1.562 V vs RHE

for $La_{0.7}K_{0.3}CoO_{3-\delta}$ was observed assisted by low resistivity due to maximum double exchange $Co3^+\text{-}O^{2+}\text{-}Co^{4+}$ pair and lowest band gap as shown in **Figure 5.3(b) and Figure 5.10**. Above 30% K doped sample, onset potential is increasing again because of the decrease in double exchange pair and increased bandgap for $La_{0.5}K_{0.5}CoO_{3-\delta}$, as onset potential is increased to 1.59V vs.RHE for $La_{0.5}K_{0.5}CoO_{3-\delta}$.

Figure. 5.12(c) shows the Tafel plot of $La_{1-x}K_xCoO_{3-\delta}$ ($0{\leq}x{\leq}0.5$) catalysts for the OER activities, the polarization curve is plotted between overpotential (η) versus the logarithm of the current density ($\log i$). Tafel plots explain the kinetics of the OER activity. The Tafel slope for $La_{1-x}K_xCoO_{3-\delta}$ ($0 \leq x \leq 0.5$) was found to be 142, 135, 129, 87 , 127, and 130 mV dec^{-1} respectively for x =0, 0.1, 0.2, 0.3, 0.4 and 0.5 samples. **Figure.5.12 (d)** shows ORR activity $La_{1-x}K_xCoO_{3-\delta}$ ($0{\leq}x{\leq}0.5$) sample. The experiment was carried out in oxygen saturated 1M KOH electrolyte at a 3mV/s scan rate and it was observed that the $La_{0.7}K_{0.3}CoO_{3-\delta}$ electrode showed superior ORR catalyst activity and onset potential was found to be 0.9V vs. RHE at 5mA/cm^2

$$ORR = \quad O_2 + 2H_2O + 4e^- \rightarrow 4OH^- \qquad (5.7)$$
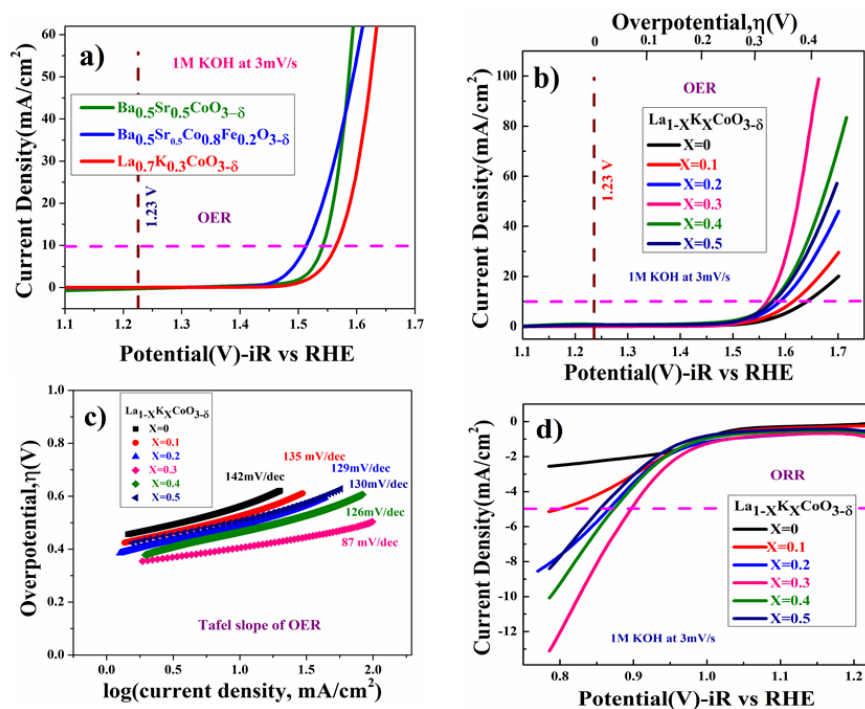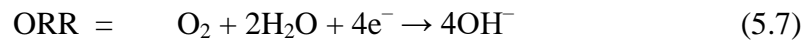
Figure 5.12 (a) OER polarization profiles of BSCF, $Ba_{0.5}Sr_{0.5}CoO_{3-\delta}$, and $La_{0.7}K_{0.3}CoO_{3-\delta}$ in 1M KOH solution (b) OER polarization profiles for the $La_{1-x}K_xCoO_{3-\delta}$ ($0 \leq x \leq 0.5$) samples obtained using a 3 mVs^{-1} scan rate in 1M KOH solution (c) respective Tafel plots for $La_{1-x}K_xCoO_{3-\delta}$ ($0 \leq x \leq 0.5$) sample (d) ORR

polarization profiles for the $La_{1-x}K_xCoO_{3-\delta}$ ($0 \leq x \leq 0.5$) samples obtained using a 3 mVs^{-1} scan rate in O_2 saturated 1M KOH solution.

## 5.3.13 EIS (Electrochemical impedance spectroscopy) and Cdl value analysis

EIS (Electrochemical impedance spectroscopy) measurements were also carried out to evaluate the charge-transfer rate of catalysts. Electrochemical impedance spectra for the $La_{1-x}K_xCoO_{3-\delta}$ ($0 \leq x \leq 0.5$) at 1.7V vs RHE are shown in **Figure. 5.13 (a)**. An equivalent circuit fit of EIS data contains a solution resistance (Rs), a charge-transfer resistance (Rct), and Double-layer Capacitance (Rcdl). A lower Rct value indicates the fastest charge transfer rate and outstanding OER activity. The Rct of $La_{0.7}K_{0.3}CoO_{3-\delta}$ (24Ω) is much smaller than that of $LaCoO_{3-\delta}$ (98Ω), this demonstrates that the 30% K doped sample has the lowest resistance. **Figure. 5.13 (b)** shows the measure Cdl values and it was found to be 3.7, 11.2 , and 22.7 mF cm^{-2} for $La_{1-x}K_xCoO_{3-\delta}$ (x = 0.1,0.3 and 0.5) samples, respectively. $La_{0.7}K_{0.3}CoO_{3-\delta}$ has the lowest Cd1, indicating. $La_{0.7}K_{0.3}CoO_{3-\delta}$ has the largest active sites for OER/ORR activities
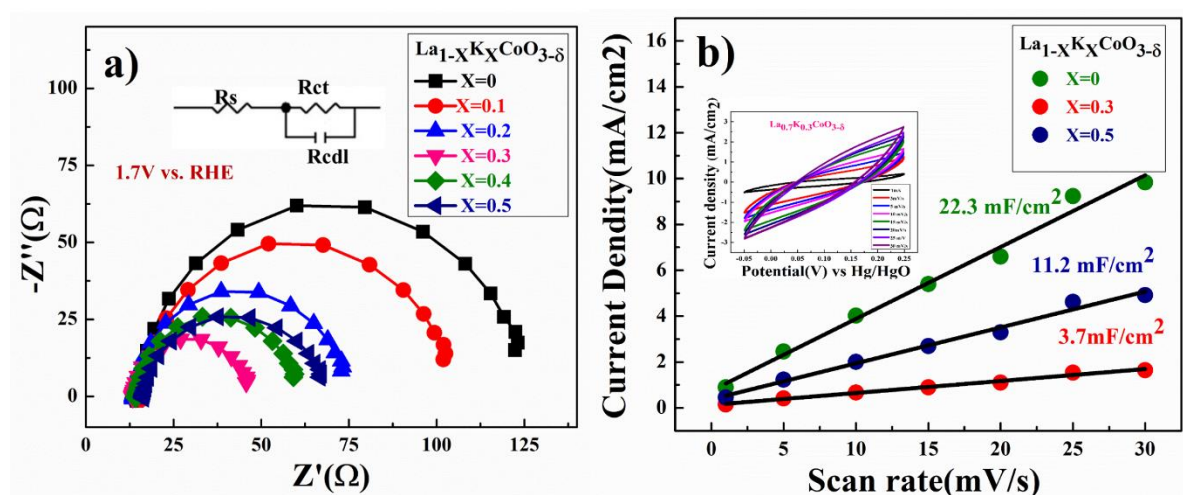
Figure 5.13. (a) Electrochemical impedance (EIS) spectra for the the $La_{1-x}K_xCoO_{3-\delta}$ ($0 \leq x \leq 0.5$) at 1.7V vs RHE (b) measure Cdl values of $La_{1-x}K_xCoO_{3-\delta}$ (x = 0.1,0.3 and 0.5)

5.3.14 Chronoamperometric stability test

The stability of the $La_{0.7}K_{0.3}CoO_{3-\delta}$ catalysts was examined by a chronoamperometric experiment. In **Figure.5.14**, $La_{0.7}K_{0.3}CoO_{3-\delta}$ showed a relatively stable current density at fixed applied potential and a current loss equivalent to ~19% was observed at 1.7V operating voltage vs. RHE in 25 hours. Insert CV figure in **Figure. 5.14,** shows cyclic stability from cyclic voltammogram up to 200 cycles. These studies demonstrate the superior stability of $La_{0.7}K_{0.3}CoO_{3-\delta}$ perovskite catalyst. The study reveals the direct relation of Physiochemical properties with the inclusion/substitution of K^+ ion in $LaCoO_{3-\delta}$ resulting in superior OER/ORR activity of the catalyst.
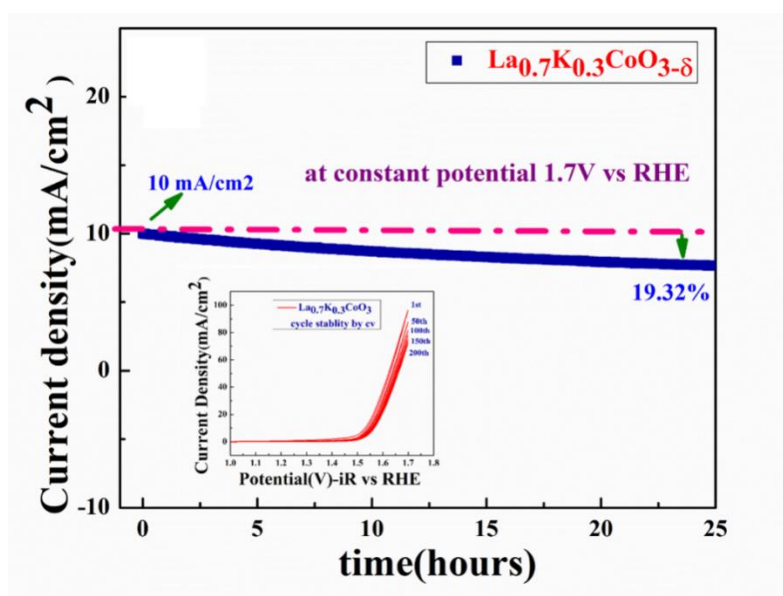
Figure 5.14 Chronoamperometric responses of $La_{0.7}K_{0.3}CoO_{3-\delta}$ electrode at constant potentials at 1.7 V vs. RHE at an initial current density of 10 mA/ cm^2. (Insert stability retention by CV

5.4 Electrochemical Charge Storage Behaviour in neutral Na_2SO_4 electrolyte

The electrochemical charge storage capacity of the present $La_{1-x}K_xCoO_{3-\delta}$ ($0 \leq x \leq 0.5$) was studied using a three-electrode configuration in a 0.5 M aqueous in neutral Na_2SO_4 electrolyte and then in a two-electrode ASC cell device configuration. Electrochemical performance of $La_{1-x}K_xCoO_{3-\delta}$ ($0 \leq x \leq 0.5$) samples were determined using cyclic voltammetry and galvanostatic charge/discharge curve. All samples of $La_{1-x}K_xCoO_{3-\delta}$ ($0 \leq x \leq 0.5$) were studied in 0.5 M Na_2SO_4 electrolytes in the voltage range of 0 to 0.7 V.

5.4.1 Bifunctional OER catalyst and supercapacitive energy storage behavior

Figure 5.15 shows comparative cyclic voltammetry of $La_{0.7}K_{0.3}CoO_{3-\delta}$ in basic I M KOH and neutral 0.5 M Na_2SO_4 electrolytes. Two distinctively different behavior was observed in term of pH-dependence; electrocatalytic (OER/ORR) behavior was observed in basic medium (1 M KOH electrolyte) and electrochemical charge storage capacity behavior was observed in aqueous 0.5 M Na_2SO_4 neutral electrolyte
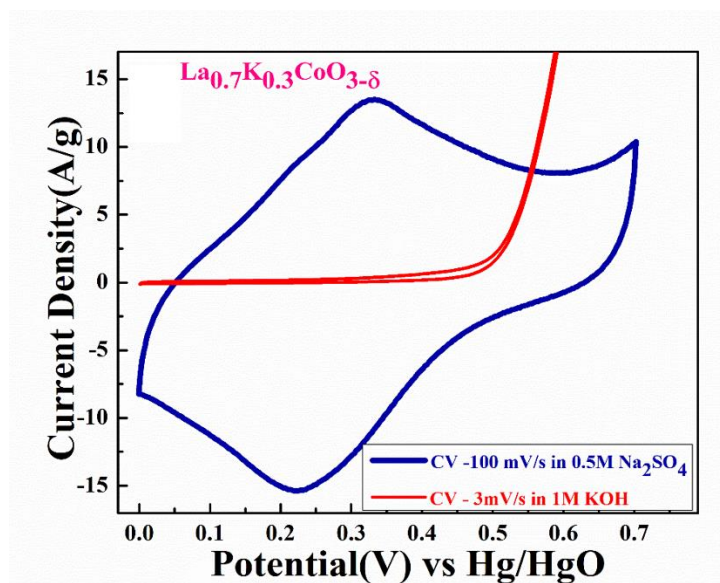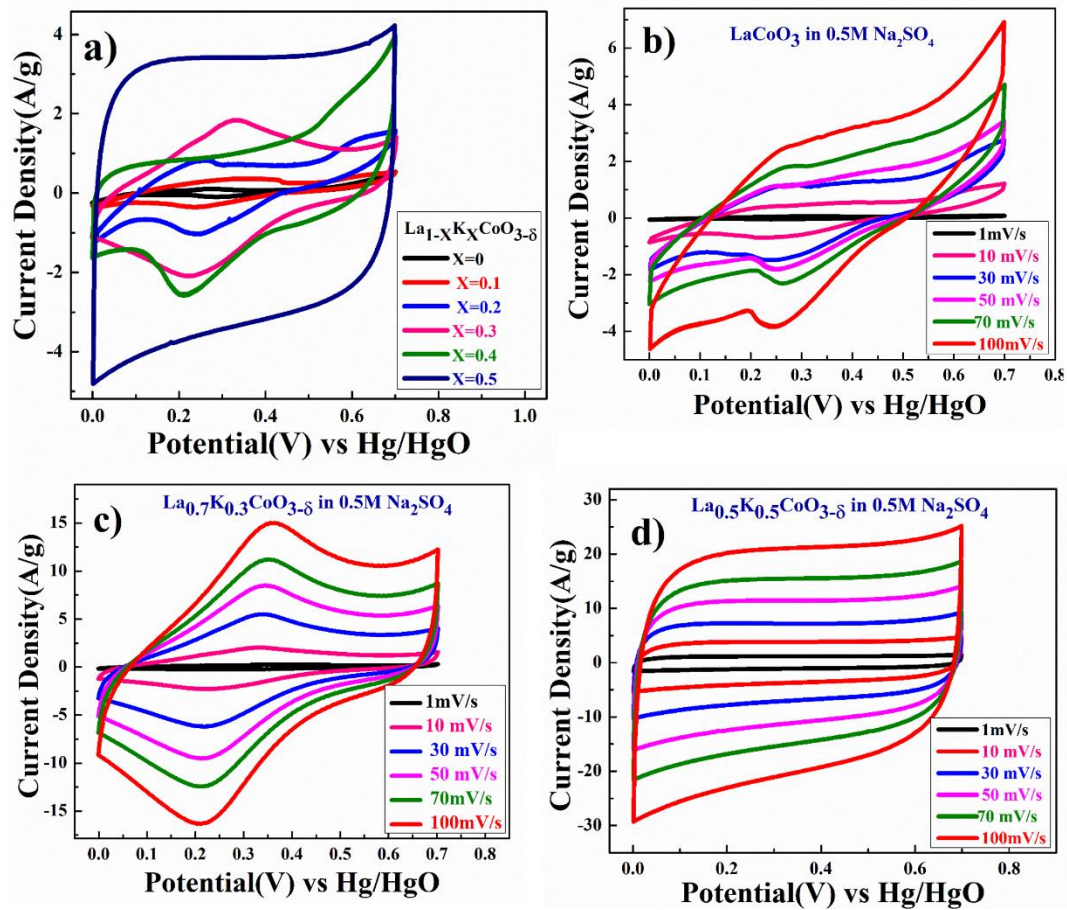

Figure 5.15. Cyclic voltammetry of $La_{0.7}K_{0.3}CoO_{3-\delta}$ material at a scan rate of 3 mV/s in 1 M KOH electrolyte and a scan rate of 10 mV/s in 0.5 M Na_2SO_4 electrolyte

5.4.2 Cyclic voltammetry study in neutral Na_2SO_4 electrolyte

Figure 5.16 (a) represents the comparative cyclic voltammetry curve for $La_{1-x}K_xCoO_{3-\delta}$ ($0 \leq x \leq 0.5$) with increasing K concentration. Pure $LaCoO_3$ shows small $Co^{2+/3+}$ redox behaviour and 30% K sample $La_{0.7}K_{0.3}CoO_{3-\delta}$ behave like battery-type charge storage materials in an aqueous, neutral 0.5 M Na_2SO_4 electrolyte. A broad peak shows $Co^{2+/3+/4+}$ redox observed simultaneously for $La_{0.7}K_{0.3}CoO_{3-\delta}$. But $La_{0.5}K_{0.5}CoO_{3-\delta}$ don't show surface redox behaviour, due to the conversion of the majority of Co^{3+} ions into Co^{4+} ion in a 50% K-doped $LaCoO_3$ sample. Cyclic Voltammetry curve for $La_{1-x}K_xCoO_{3-\delta}$ (x = 0, 0.3 and 0.5) with different scan rates are

shown in **Figure 5.16 (b-d)** respectively. For x = 0.3 composition, $La_{0.7}K_{0.3}Co_{0.55}^{4+}Co_{0.46}^{3+}O_{2.97}$, with an almost equal concentration of Co^{4+} and Co^{3+} state, both $Co^{4+/3+}$ and $Co^{3+/2+}$ redox peak seem to operate in very close voltage range representing a clean diffusion-controlled behavior of the electrode.

Figure 5.16 (a) Comparative Cyclic voltammetry of $La_{1-x}K_xCoO_{3-\delta}$ ($0 \leq x \leq 0.5$) material at scan rate 10 mV/s in 0.5 M Na_2SO_4 electrolyte (b-d) cyclic voltammetry of $La_{1-x}K_xCoO_{3-\delta}$ (x =0, 0.3, 0.5) material in in 0.5 M Na_2SO_4 electrolyte

However, a low capacity output results for the electrode. The quasi rectangular shape of the curve suggests the dominance of pseudo-capacitance behaviour coupled with EDLC type capacitance for $La_{0.5}K_{0.5}CoO_{3-\delta}$. The specific capacitance C (F/g) was calculated to understand the electrochemical performance of the working electrode as represented by **equation (5.8)**.

$$Csp = \frac{\int I(V)dV}{mV\nu} \tag{5.8}$$

Where I (A) is the cathodic current, v (V·s^{-1}) is the scan rate, m (g) is the mass of active material, and V (V) is the sweep potential window. [35]The capacitance values were found to be 87 F/g, 126 F/g, 148F/g, 191 F/g, 311 F/g, and 378 F/g respectively at 1mV/s for the La$_{1-x}$K$_x$CoO$_{3-\delta}$ (X= 0, 0.1, 0.2, 0.3, 04 and 0.5) electrodes respectively.

5.4.3 b value (Kinetics) in Na$_2$SO$_4$ aqueous electrolyte

The area under the curve from the CV plot represents the total charge stored through Faradic and non-Faradic reactions that occurred on the electrode surface. The current behavior is generally followed by a power law and it is related to scan rate as depicted by the following equation.

$$i = av^b \tag{5.9}$$

Where a and b are the variables that govern the nature of intercalation, i is the current (A), and ϑ is the scan rate (V/s). The value of b lies between 0.5 to 1, b = 0.5 stands for the diffusion control reaction or battery type behavior, and b = 1 stands for the diffusion-controlled faradic process and hybrid charge storage mechanism involving charge transfer with surface/subsurface atoms. [23, 24, 27]

Figure 5.17 shows the kinetics of the charge storage mechanism of La$_{1-x}$K$_x$CoO$_{3-\delta}$ ($0 \leq x \leq 0.5$) in Na$_2$SO$_4$ aqueous electrolyte analyzed from CV curves. The lowest b value of 0.714 was found in La$_{0.7}$K$_{0.3}$CoO$_{3-\delta}$, which means involvement of diffusion control faradic process, and the b value was found to be 0.843 for La$_{0.5}$K$_{0.5}$CoO$_{3-\delta}$ which means surface control charge storage was more prominent over diffusion control in the sample
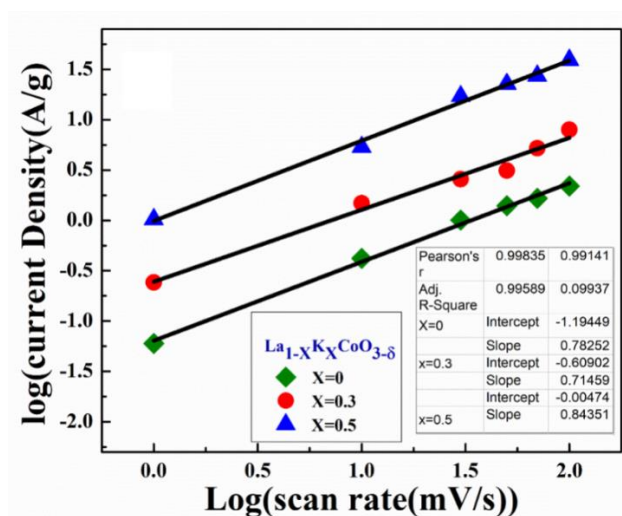
Figure 5.17 Plot of linear relationship between log (peak current) and log (scan rate) at two different scan rate regions of of of La$_{1-x}$K$_x$CoO$_{3-\delta}$ (x =0, 0.3, 0.5)

5.4.4 Dunn method and Kinetics analysis

Figure.5.18.a) Voltammetry sweep rate dependence can distinguish quantitatively the capacitive contribution to the current response of $La1_{-x}K_xCoO_{3-\delta}$ (x =0, 0.3, 0.5) in Na_2SO_4 aqueous electrolyte. The current response at a fixed potential as being the combination of two separate mechanisms, surface capacitive effects, and diffusion-controlled insertion.

$$i(\upsilon) = k_1\upsilon + k_2\upsilon^{\frac{1}{2}} \tag{5.10}$$

For more understanding, **equation5.10** was modified

$$\frac{i(\upsilon)}{\upsilon^{\frac{1}{2}}} = \frac{k_1}{\upsilon^{\frac{1}{2}}} + k_2 \tag{5.11}$$

In **Equations 5.11,** $k_1\upsilon$ and $k_2\upsilon^{1/2}$ explain the current contributions from the surface capacitive effects and the diffusion-controlled intercalation process, respectively. Thus after the determination k_1 and k_2, it can be able to quantify, at specific potentials, the fraction of the current due to each of these contributions.[23,24,27]
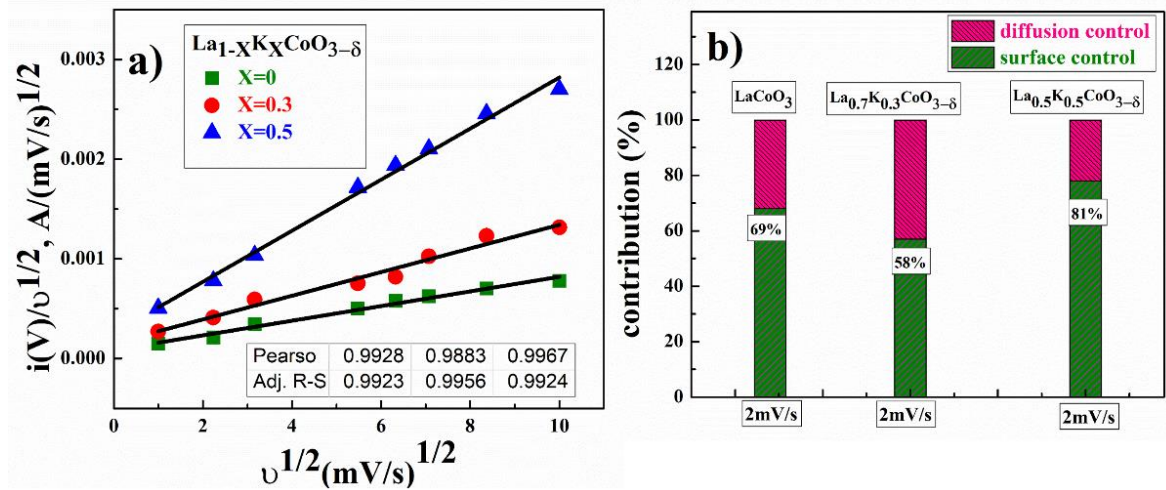
Figure 5.18 (a) Plot of power's law of charged state at a potential and discharged state at a potential of $La_{1-x}K_xCoO_{3-\delta}$ (x =0, 0.3, 0.5) (b) Contribution of diffusive and capacitive at different scan rates contribution of of $La_{1-x}K_xCoO_{3-\delta}$ (x =0, 0.3, 0.5) at 2mV/s

After Linear fitting, k_1 and k_2 are determined from the slope and intercept of the y-axis. The representative curve of $i(V)/\upsilon^{1/2}$ vs. $\upsilon^{1/2}$ is in **Figure 5.18 (a)**. Represent the contribution of surface capacitance and diffusion-controlled interaction at 2mV scan

rate of $La_{1-x}K_xCoO_{3-\delta}$ (x =0, 0.3, 0.5) in Na_2SO_4 aqueous electrolyte in **Figure5.18.(b),** it is clearly shown $La_{0.7}K_{0.3}CoO_{3-\delta}$ has more diffusion control redox behavior (battery type) and $La_{0.5}K_{0.5}CoO_{3-\delta}$ has more surface control capacitive nature, but $La_{0.5}K_{0.5}CoO_{3-\delta}$ has most specific capacitance value.

5.4.5 Charge discharge (plot V vs. time) analysis in Na_2SO_4 aqueous electrolyte

Charge discharge measurement (Potential (V) vs. time (t)) was carried out at constant current by chronopotentiometry. The gravimetric capacitance value was calculated from the Potential (V) vs. time (t) plot by using the following equation given below. [23, 27]

$$C = \frac{I \triangle t}{mV} \tag{5.12}$$

Where I (A) is the applying constant current, Δt (s) is the discharge time, m (g) is active mass, and V represents the operating potation window. [43]
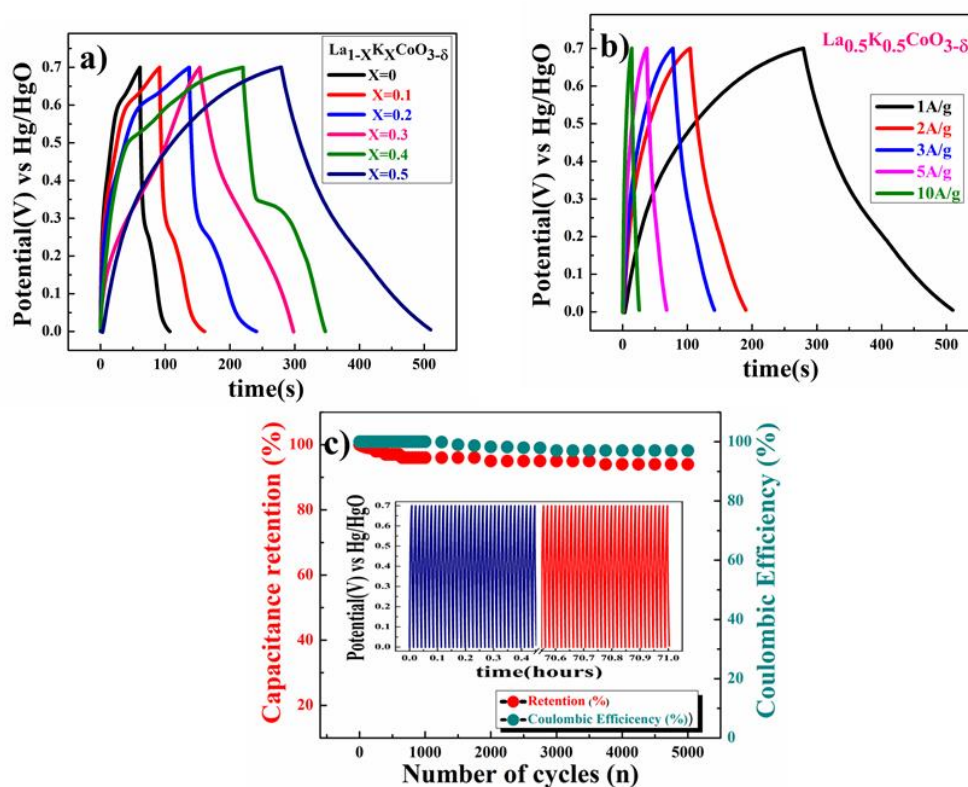

Figure 5.19. (a) Charge discharge (plot V vs. time) of $La_{1-x}K_xCoO_{3-\delta}$ ($0 \leq x \leq 0.5$) electrode at 1A/g in 0.5 M Na_2SO_4 (b) charge-discharge (plot potential (V) vs. time(t)) of $La_{0.5}K_{.5}CoO_{3-\delta}$ electrode 0.5M Na_2SO_4 (c) capacitive retention and columbic efficacy with cycle number

The gravimetric capacitance of the $La_{1-x}K_xCoO_{3-\delta}$ ($0 \leq x \leq 0.5$) electrode from the charge-discharge plot is shown in **Figure.5.19 (a)** and at the current rate of 1A/g are their values were found to be 87 F/g, 126 F/g, 148F/g, 191 F/g, 311 F/g, and 378 F/g respectively for x = 0, 0.1, 0.2, 0.3, 04 and 05 samples. Gravimetric capacitance values in **Figure5.19. (b)** are found to 378 F/g, 282F/g, 221F/g, 163F/g, 74F/g respectively at constant current of 1A/g, 2A/g, 3A/g, 5A/g, and 10A/g for. Up to 94 % capacitive retention and columbic efficacy up to 97% were obtained for continuous 5000 cycles of charge/discharge for the $La_{0.5}K_{0.5}CoO_{3-\delta}$ electrode at 10A/g constant current as shown in **Figure5.18 (c).**

5.4.6 EIS (Electrochemical Impedance Spectroscopy) analysis in Na_2SO_4 aqueous electrolyte

$La_{0.5}K_{0.5}CoO_{3-\delta}$ electrode. EIS plot (Nyquist) in the frequency range (1MHz to 0.1Hz) at 10 mV applied voltage of $La_{1-x}K_xCoO_{3-\delta}$ ($0 \leq x \leq 0.5$) electrode is shown in **Figure 5.20** Rs (contact resistance), Cdl (double layer capacitance), Rct (charge-transfer resistance), W (Warburg component), and C1 (specific capacitance) denote different types of resistance. The small semicircle of $La_{0.5}K_{0.5}CoO_{3-\delta}$ in the high-frequency region (indicating lower Rct, 3.859 Ω) and the straight line with a larger slope in the low-frequency region imply the excellent capacitance characteristics of the hybrid supercapacitors
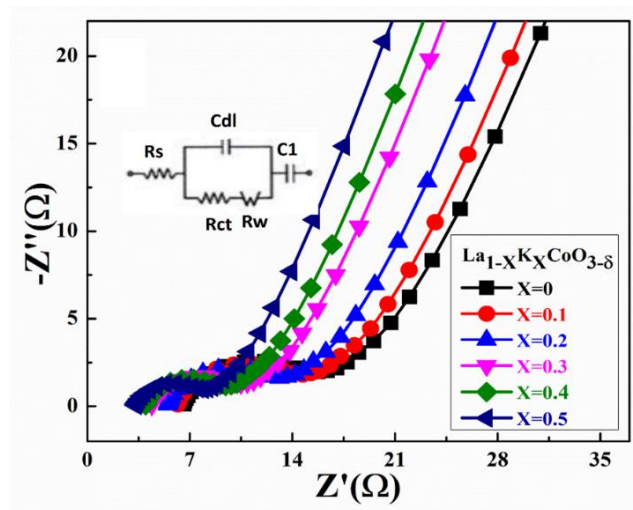
Figure 5.20 Impedance spectroscopy (EIS) at 10mV AC applied voltage(V) from 1MHz to 0.01 Hz

5.4.7 Full cell (La$_{0.5}$K$_{0.5}$CoO$_{3-\delta}$ // AC (Activated carbon) electrochemical analysis in Na$_2$SO$_4$ aqueous electrolyte
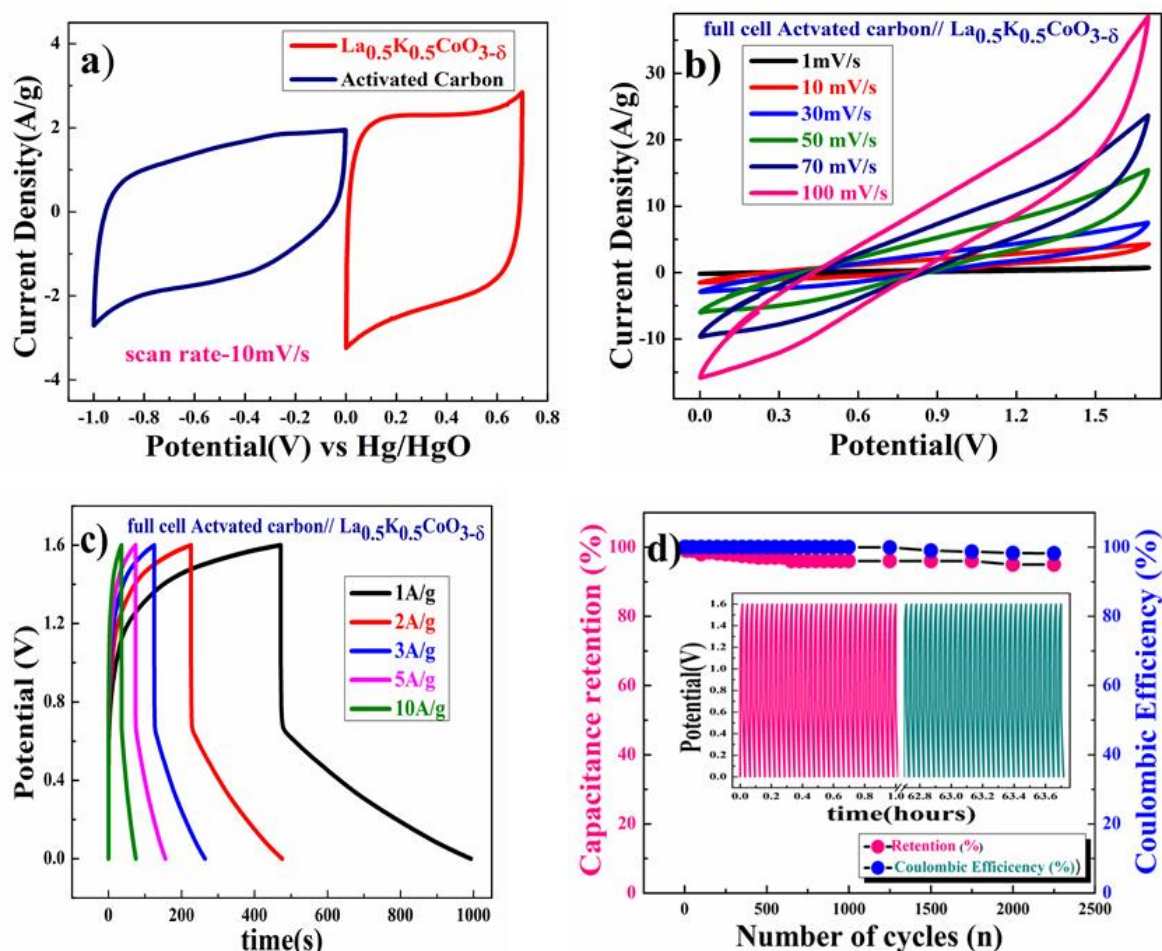
Figure 5.21 . showing full cell (ASCs) performances of activated carbon vs. La$_{0.5}$ K$_{0.5}$CoO$_{3-\delta}$ electrode; (a) CV of individual electrodes at 10 mV/s respect to Hg/HgO electrode in 0.5 M Na$_2$SO$_4$, (b) CV at different scan rate of ASCs in 0.5 M Na$_2$SO$_4$ (c) charge-discharge in 0.5 M Na$_2$SO$_4$, , (d) Capacitance retention and coulombic efficiency with 2500 cycle at 10 A/g constant current of the full cell

To understand the real charge storage behaviour of La$_{0.5}$K$_{0.5}$CoO$_{3-\delta}$ relative to AC (Activated carbon), two electrode ASCs (Asymmetry Supercapacitors) mode measurements have been conducted in 0.5 M Na$_2$SO$_4$ neutral electrolyte. To determine the maximum specific capacitance during the full test, the storage capacity of positive and negative electrodes need to be balanced as per the following equation:

$$\frac{1}{C_{total}} = \frac{1}{C_{positive}} + \frac{1}{C_{negative}}$$

(5.13)

For balancing the charge storage capacity of the cell, the mass ratio (m^+/m^-) of positive and negative electrode material was measured using the following equation:

$$\frac{m^+}{m^-} = \frac{C_- \times \Delta E_-}{C_+ \times \Delta E_+} \tag{5.14}$$

$m^+, m^-, C_+, C_-, \Delta E_+, \Delta E_-$ are mass, specific capacitance, and potential window of positive and negative electrodes estimated by three-electrode measurement.[36-37]

Figure 5.21. (a) shows the CV plot at a 10 mV/s scan rate where AC (activate carbon) acts as the negative electrode and $La_{0.5}K_{0.5}CoO_{3-\delta}$ acts as the Positive electrode. The calculated mass ratio ($\frac{m^+}{m^-}$) was found 1: 1.4 for the asymmetric cell and the weight of the active materials was taken to be 2.4 mg (excluding the weight of acetylene black and PVDF). **Figure5.21. (b)** demonstrate the CV curve of $La_{0.5}K_{0.5}CoO_{3-\delta}$ //AC two-electrode in ASCs mode at different scan rates, ranging from 1mV/s to 100mV/s in potential window 1.7 V.

Figure 5.21. (c) subsequently, shows the charge/discharge curve conducted for measuring the capacitance of the electrode, and capacitance values were calculated by using **equation 5.12**. Capacitances for $La_{0.5}K_{0.5}CoO_{3-\delta}$ electrodes were found to be 308F/g, 287F/g, 238F/g, 209F/g and 162F/g at current densities of 1A/g, 2A/g, 3A/g, and 5A/g respectively. **Figure 5.21 (d)** shows that the Coulombic efficiency of two electrode full cells has lost only 3% with higher capacity retention close to 90.5% of its initial value after 2500cycles at applied constant current equivalent to 5A/g. Specific energy and specific power of asymmetric capacitors were calculated using the following equations:[23,27]

5.4.8   Full cell   ($La_{0.5}K_{0.5}CoO_{3-\delta}$ // AC (Activated carbon) EIS (Electrochemical Impedencnce Spectroscopy) analysis in Na_2SO_4 aqueous electrolyte

Figure 5.22 shows the EIS plot (Nyquist) in the frequency range (1MHz to 0.1Hz) at 10 mV applied voltage) confirming superior charge transfer and higher capacitance of $La_{0.5}K_{0.5}CoO_{3-\delta}$ //AC) in full cell mode.
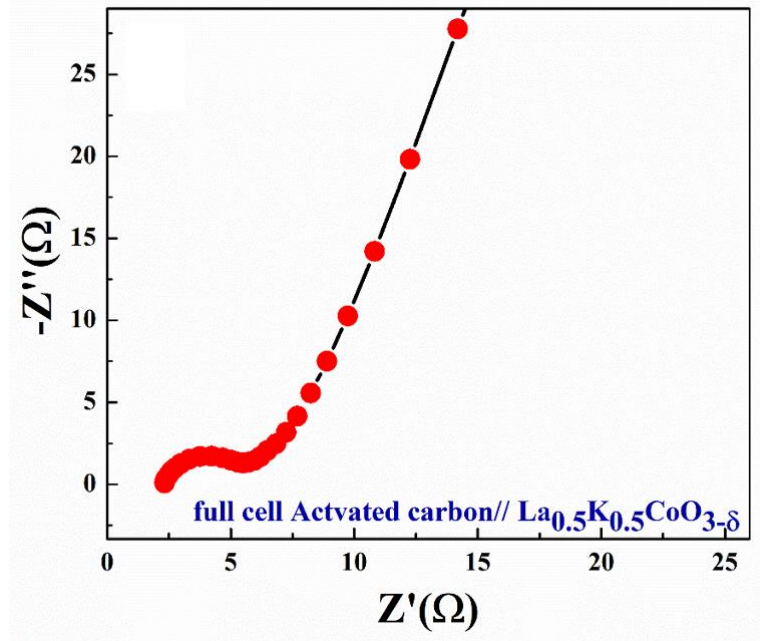
Figure 5.22. showing EIS at 10 mV applied voltage, full cell (ASCs) performances of activated carbon vs. $La_{0.5}K_{0.5}CoO_{3-\delta}$ electrode

5.4.9 Full cell ($La_{0.5}K_{0.5}CoO_{3-\delta}$ // AC (Activated carbon) of specific energy vs. specific power in Na_2SO_4 aqueous electrolyte

.

$$E(Wh/kg) = \frac{1}{2}\frac{C_{ASCs}}{3.6}V^2 \tag{5.15}$$

$$P(W/kg) = \frac{E*3600}{t_{dis}} \tag{5.16}$$

Where C_{ASCs} is specific capacitance, V is operating voltage and t_{dis} is discharge time. [37]

Figure 5.23 shows a plot of specific energy vs. specific power with different constant current rates. Resultant values show the highest specific energy equivalent to 109 Wh/kg at 1A/g current density and specific power of ~1204W/kg. Maximum specific power equivalent to ~6884 W/kg was obtained when specific energy was reduced to ~57 Wh/kg at 10A/g of current density
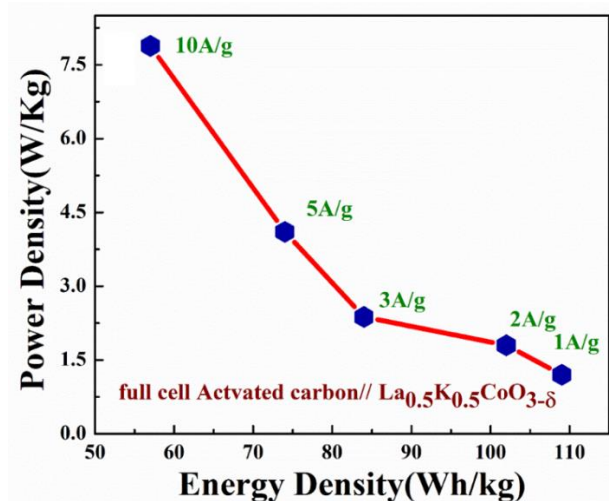
Figure 5.23. showing Ragone plot full cell (ASCs) performances of activated carbon vs. $La_{0.5}K_{0.5}CoO_{3-\delta}$ electrode

5.5 Conclusions:

In summary, $La_{1-x}K_xCoO_{3-\delta}$ ($0 \leq x \leq 0.5$) shows a pH-dependent bifunctional electrocatalyst (OER/ORR) and electrochemical charge storage behavior in different electrolytes. The as-prepared K doped $La_{1-x}K_xCoO_{3-\delta}$ ($0 \leq x \leq 0.5$) possesses improved charge storage kinetics and activities as electrode material for supercapacitors and the oxygen evolution reaction (OER), oxygen reduction reaction (ORR) for the metal-air battery. 30 % K doped p-type $La_{0.7}K_{0.3}CoO_{3-\delta}$ show superior OER activity with an overpotential of 335 at $10mA/cm^2$ current rate in 1M KOH electrolyte. The double exchange mechanism enhances OER catalytic properties and additionally, improves charge storage kinetics and activities as electrode material $La_{1-x}K_xCoO_{3-\delta}$ ($0 \leq x \leq 0.5$) for supercapacitors application. High Gravimetric capacitance of $La_{0.5}K_{0.5}CoO_{3-\delta}$ electrode equivalent to 378 F/g, 282F/g, 221F/g, 163F/g, 74F/g was found at constant current of 1A/g, 2A/g, 3A/g, 5A/g, and 10A/g respectively in neutral 0.5M Na_2SO_4 electrolyte. Up to 94% capacitive retention and columbic efficacy (97%) was obtained for continuous 5000 cycles of charge/discharge for $La_{0.5}K_{0.5}FeO_{3-\delta}$ electrode. Gravimetric capacitance values of ASCs (Activated Carbon// $La_{0.5}K_{0.5}FeO_{3-\delta}$) are Capacitances for $La_{0.5}K_{0.5}CoO_{3-\delta}$ electrodes were found to be 308 F/g, 287 F/g, 238 F/g, 209 F/g and 162 F/g at current densities of 1 A/g, 2 A/g, 3 A/g, 5 A/g and 10 A/g respectively in neutral 0.5 M Na_2SO_4 electrolyte. Maximum specific power equivalent to ~6884 W/kg was obtained when specific energy was reduced to ~57 Wh/kg at 10A/g of current density.